Pulsatile motion of the trabecular meshwork in healthy human subjects quantified by phase-sensitive optical coherence tomography

Peng Li,[1] Tueng T. Shen,[1,2] Murray Johnstone,[2] and Ruikang K. Wang[1,2,*]

[1]*Departments of Bioengineering, University of Washington, Seattle, WA 98195, USA*
[2]*Department of Ophthalmology, University of Washington, Seattle, WA 98195, USA*
* wangrk@uw.edu

Abstract: Aqueous leaves the anterior chamber of eye by passing through the trabecular meshwork (TM), a tissue thought to be responsible for increased outflow resistance in glaucoma. Motion assessment could permit characterization of TM biomechanical properties necessary to maintain intra-ocular pressure (IOP) within a narrow homeostatic range. In this paper, we report the first in vivo identification of TM motion in humans. We use a phase-sensitive optical coherence tomography (PhS-OCT) system with sub-nanometer sensitivity to detect and image dynamic pulse-induced TM motion. To permit quantification of TM motion and relationships we develop and apply a phase compensation algorithm permitting removal of the otherwise evitable confounding effects of bulk motion. Twenty healthy human eyes from 10 subjects are imaged. The results permit visualization of pulsatile TM motion visualization by PhS-OCT; correlation with the digital/cardiac pulse is highly significant. The correlation permits assessment of the phase lag and time delay between TM motion and the cardiac pulse. In this study, we find that the digital pulse leads the pulsatile TM motion by a mean phase of 3.53 ± 0.48 rad and a mean time of 0.5 ± 0.14 s in the fundamental frequency. A significant linear relationship is present between the TM phase lag and the heart rate (p value < 0.05). The TM phase lag is also affected by age, the relationship not quite reaching significance in the current study. PhS-OCT reveals pulse-induced motion of the TM that may provide insights into the biomechanics of the tissues involved in the regulation of IOP.

©2013 Optical Society of America

OCIS codes: (170.4500) Optical coherence tomography; (170.0110) Imaging systems; (170.3880) Medical and biological imaging; (170.4470) Ophthalmology.

References and links

1. L. S. Wilson, D. E. Robinson, and M. J. Dadd, "Elastography--the movement begins," Phys. Med. Biol. **45**(6), 1409–1421 (2000).
2. J. F. Greenleaf, M. Fatemi, and M. Insana, "Selected methods for imaging elastic properties of biological tissues," Annu. Rev. Biomed. Eng. **5**(1), 57–78 (2003).
3. J. Ophir, S. Alam, B. Garra, F. Kallel, E. Konofagou, T. Krouskop, C. Merritt, R. Righetti, R. Souchon, S. Srinivasan, and T. Varghese, "Elastography: Imaging the elastic properties of soft tissues with ultrasound," J. Med. Ultrasound **29**(4), 155–171 (2002).
4. R. J. Dickinson and C. R. Hill, "Measurement of soft tissue motion using correlation between A-scans," Ultrasound Med. Biol. **8**(3), 263–271 (1982).
5. D. Huang, E. A. Swanson, C. P. Lin, J. S. Schuman, W. G. Stinson, W. Chang, M. R. Hee, T. Flotte, K. Gregory, C. A. Puliafito, and et, "Optical coherence tomography," Science **254**(5035), 1178–1181 (1991).
6. P. H. Tomlins and R. K. Wang, "Theory, developments and applications of optical coherence tomography," J. Phys. D Appl. Phys. **38**(15), 2519–2535 (2005).
7. A. F. Fercher, W. Drexler, C. K. Hitzenberger, and T. Lasser, "Optical coherence tomography - principles and applications," Rep. Prog. Phys. **66**(2), 239–303 (2003).
8. J. Schmitt, "OCT elastography: imaging microscopic deformation and strain of tissue," Opt. Express **3**(6), 199–

211 (1998).

9. R. Chan, A. Chau, W. Karl, S. Nadkarni, A. Khalil, N. Iftimia, M. Shishkov, G. Tearney, M. Kaazempur-Mofrad, and B. Bouma, "OCT-based arterial elastography: robust estimation exploiting tissue biomechanics," Opt. Express **12**(19), 4558–4572 (2004).

10. J. Rogowska, N. A. Patel, J. G. Fujimoto, and M. E. Brezinski, "Optical coherence tomographic elastography technique for measuring deformation and strain of atherosclerotic tissues," Heart **90**(5), 556–562 (2004).

11. R. K. Wang, Z. Ma, and S. J. Kirkpatrick, "Tissue Doppler optical coherence elastography for real time strain rate and strain mapping of soft tissue," Appl. Phys. Lett. **89**(14), 144103 (2006).

12. R. K. Wang, S. Kirkpatrick, and M. Hinds, "Phase-sensitive optical coherence elastography for mapping tissue microstrains in real time," Appl. Phys. Lett. **90**(16), 164105 (2007).

13. X. Liang, A. L. Oldenburg, V. Crecea, E. J. Chaney, and S. A. Boppart, "Optical micro-scale mapping of dynamic biomechanical tissue properties," Opt. Express **16**(15), 11052–11065 (2008).

14. X. Liang, S. G. Adie, R. John, and S. A. Boppart, "Dynamic spectral-domain optical coherence elastography for tissue characterization," Opt. Express **18**(13), 14183–14190 (2010).

15. P. Li, A. Liu, L. Shi, X. Yin, S. Rugonyi, and R. K. Wang, "Assessment of strain and strain rate in embryonic chick heart in vivo using tissue Doppler optical coherence tomography," Phys. Med. Biol. **56**(22), 7081–7092 (2011).

16. P. Li, X. Yin, L. Shi, S. Rugonyi, and R. K. Wang, "*In vivo* functional imaging of blood flow and wall strain rate in outflow tract of embryonic chick heart using ultrafast spectral domain optical coherence tomography," J. Biomed. Opt. **17**(9), 096006 (2012).

17. R. K. Wang and A. L. Nuttall, "Phase-sensitive optical coherence tomography imaging of the tissue motion within the organ of Corti at a subnanometer scale: a preliminary study," J. Biomed. Opt. **15**(5), 056005 (2010).

18. P. Li, R. Reif, Z. Zhi, E. Martin, T. T. Shen, M. Johnstone, and R. K. Wang, "Phase-sensitive optical coherence tomography characterization of pulse-induced trabecular meshwork displacement in ex vivo nonhuman primate eyes," J. Biomed. Opt. **17**(7), 076026 (2012).

19. S. G. Adie, X. Liang, B. F. Kennedy, R. John, D. D. Sampson, and S. A. Boppart, "Spectroscopic optical coherence elastography," Opt. Express **18**(25), 25519–25534 (2010).

20. C. Sun, B. Standish, and V. X. Yang, "Optical coherence elastography: current status and future applications," J. Biomed. Opt. **16**(4), 043001 (2011).

21. Y. Zhao, Z. Chen, Z. Ding, H. Ren, and J. S. Nelson, "Real-time phase-resolved functional optical coherence tomography by use of optical Hilbert transformation," Opt. Lett. **27**(2), 98–100 (2002).

22. R. K. Wang and Z. Ma, "Real-time flow imaging by removing texture pattern artifacts in spectral-domain optical Doppler tomography," Opt. Lett. **31**(20), 3001–3003 (2006).

23. P. Li, L. An, G. Lan, M. Johnstone, D. Malchow, and R. K. Wang, "Extended imaging depth to 12 mm for 1050-nm spectral domain optical coherence tomography for imaging the whole anterior segment of the human eye at 120-kHz A-scan rate," J. Biomed. Opt. **18**(1), 016012 (2013).

24. C. I. Phillips, S. Tsukahara, O. Hosaka, and W. Adams, "Ocular pulsation correlates with ocular tension: the choroid as piston for an aqueous pump?" Ophthalmic Res. **24**(6), 338–343 (1992).

25. P. L. Kaufman and C. A. Rasmussen, "Advances in glaucoma treatment and management: outflow drugs," Invest. Ophthalmol. Vis. Sci. **53**(5), 2495–2500 (2012).

26. R. F. Ramos and W. D. Stamer, "Effects of cyclic intraocular pressure on conventional outflow facility," Invest. Ophthalmol. Vis. Sci. **49**(1), 275–281 (2008).

27. R. F. Ramos, G. M. Sumida, and W. D. Stamer, "Cyclic mechanical stress and trabecular meshwork cell contractility," Invest. Ophthalmol. Vis. Sci. **50**(8), 3826–3832 (2009).

28. S. J. Tumminia, K. P. Mitton, J. Arora, P. Zelenka, D. L. Epstein, and P. Russell, "Mechanical stretch alters the actin cytoskeletal network and signal transduction in human trabecular meshwork cells," Invest. Ophthalmol. Vis. Sci. **39**(8), 1361–1371 (1998).

29. C. Luna, G. Li, P. B. Liton, D. L. Epstein, and P. Gonzalez, "Alterations in gene expression induced by cyclic mechanical stress in trabecular meshwork cells," Mol. Vis. **15**, 534–544 (2009).

30. P. B. Liton, X. Liu, P. Challa, D. L. Epstein, and P. Gonzalez, "Induction of TGF-beta1 in the trabecular meshwork under cyclic mechanical stress," J. Cell. Physiol. **205**(3), 364–371 (2005).

31. P. B. Liton, C. Luna, M. Bodman, A. Hong, D. L. Epstein, and P. Gonzalez, "Induction of IL-6 expression by mechanical stress in the trabecular meshwork," Biochem. Biophys. Res. Commun. **337**(4), 1229–1236 (2005).

32. E. R. Tamm, P. Russell, D. L. Epstein, D. H. Johnson, and J. Piatigorsky, "Modulation of myocilin/TIGR expression in human trabecular meshwork," Invest. Ophthalmol. Vis. Sci. **40**(11), 2577–2582 (1999).

33. K. P. Mitton, S. J. Tumminia, J. Arora, P. Zelenka, D. L. Epstein, and P. Russell, "Transient loss of alphaB-crystallin: an early cellular response to mechanical stretch," Biochem. Biophys. Res. Commun. **235**(1), 69–73 (1997).

34. B. Junglas, S. Kuespert, A. A. Seleem, T. Struller, S. Ullmann, M. Bösl, A. Bosserhoff, J. Köstler, R. Wagner, E. R. Tamm, and R. Fuchshofer, "Connective tissue growth factor causes glaucoma by modifying the actin cytoskeleton of the trabecular meshwork," Am. J. Pathol. **180**(6), 2386–2403 (2012).

35. C. Luna, G. Li, J. Qiu, P. Challa, D. L. Epstein, and P. Gonzalez, "Extracellular release of ATP mediated by cyclic mechanical stress leads to mobilization of AA in trabecular meshwork cells," Invest. Ophthalmol. Vis. Sci. **50**(12), 5805–5810 (2009).

36. J. M. B. Bradley, M. J. Kelley, A. Rose, and T. S. Acott, "Signaling Pathways Used in Trabecular Matrix

Metalloproteinase Response to Mechanical Stretch," Invest. Ophthalmol. Vis. Sci. **44**(12), 5174–5181 (2003).

37. V. Vittal, A. Rose, K. E. Gregory, M. J. Kelley, and T. S. Acott, "Changes in gene expression by trabecular meshwork cells in response to mechanical stretching," Invest. Ophthalmol. Vis. Sci. **46**(8), 2857–2868 (2005).
38. T. S. Acott and M. J. Kelley, "Extracellular matrix in the trabecular meshwork," Exp. Eye Res. **86**(4), 543–561 (2008).
39. K. E. Keller, M. Aga, J. M. Bradley, M. J. Kelley, and T. S. Acott, "Extracellular matrix turnover and outflow resistance," Exp. Eye Res. **88**(4), 676–682 (2009).
40. W. D. Stamer and T. S. Acott, "Current understanding of conventional outflow dysfunction in glaucoma," Curr. Opin. Ophthalmol. **23**(2), 135–143 (2012).
41. D. WuDunn, "The effect of mechanical strain on matrix metalloproteinase production by bovine trabecular meshwork cells," Curr. Eye Res. **22**(5), 394–397 (2001).
42. J. M. Bradley, M. J. Kelley, X. Zhu, A. M. Anderssohn, J. P. Alexander, and T. S. Acott, "Effects of mechanical stretching on trabecular matrix metalloproteinases," Invest. Ophthalmol. Vis. Sci. **42**(7), 1505–1513 (2001).
43. K. E. Keller, M. J. Kelley, and T. S. Acott, "Extracellular matrix gene alternative splicing by trabecular meshwork cells in response to mechanical stretching," Invest. Ophthalmol. Vis. Sci. **48**(3), 1164–1172 (2007).
44. M. A. Johnstone, "The aqueous outflow system as a mechanical pump: evidence from examination of tissue and aqueous movement in human and non-human primates," J. Glaucoma **13**(5), 421–438 (2004).
45. E. H. Zhou, R. Krishnan, W. D. Stamer, K. M. Perkumas, K. Rajendran, J. F. Nabhan, Q. Lu, J. J. Fredberg, and M. Johnson, "Mechanical responsiveness of the endothelial cell of Schlemm's canal: scope, variability and its potential role in controlling aqueous humour outflow," J. R. Soc. Interface **9**(71), 1144–1155 (2012).
46. R. Clark, A. Nosie, T. Walker, J. A. Faralli, M. S. Filla, G. Barrett-Wilt, and D. M. Peters, "Comparative genomic and proteomic analysis of cytoskeletal changes in dexamethasone-treated trabecular meshwork cells," Mol. Cell. Proteomics **12**(1), 194–206 (2013).
47. M. S. Filla, M. K. Schwinn, A. K. Nosie, R. W. Clark, and D. M. Peters, "Dexamethasone-associated cross-linked actin network formation in human trabecular meshwork cells involves β3 integrin signaling," Invest. Ophthalmol. Vis. Sci. **52**(6), 2952–2959 (2011).
48. S. O'Reilly, N. Pollock, L. Currie, L. Paraoan, A. F. Clark, and I. Grierson, "Inducers of cross-linked actin networks in trabecular meshwork cells," Invest. Ophthalmol. Vis. Sci. **52**(10), 7316–7324 (2011).
49. J. A. Last, T. Pan, Y. Ding, C. M. Reilly, K. Keller, T. S. Acott, M. P. Fautsch, C. J. Murphy, and P. Russell, "Elastic modulus determination of normal and glaucomatous human trabecular meshwork," Invest. Ophthalmol. Vis. Sci. **52**(5), 2147–2152 (2011).
50. P. Russell and M. Johnson, "Elastic modulus determination of normal and glaucomatous human trabecular meshwork," Invest. Ophthalmol. Vis. Sci. **53**(1), 117 (2012).
51. S. M. Thomasy, J. A. Wood, P. H. Kass, C. J. Murphy, and P. Russell, "Substratum stiffness and latrunculin B regulate matrix gene and protein expression in human trabecular meshwork cells," Invest. Ophthalmol. Vis. Sci. **53**(2), 952–958 (2012).
52. M. Johnstone, E. Martin, and A. Jamil, "Pulsatile flow into the aqueous veins: Manifestations in normal and glaucomatous eyes," Exp. Eye Res. **92**(5), 318–327 (2011).
53. M. A. Johnstone, "A New Model Describes an Aqueous Outflow Pump and Explores Causes of Pump Failure in Glaucoma," in *Glaucoma. Essentials in Ophthalmology*, F. Grehn and R. Stamper, eds. (Springer Berlin Heidelberg, 2006), pp. 3–34.
54. E. B. Suson and R. O. Schultz, "Blood in schlemm's canal in glaucoma suspects. A study of the relationship between blood-filling pattern and outflow facility in ocular hypertension," Arch. Ophthalmol. **81**(6), 808–812 (1969).
55. B. A. Francis, K. Singh, S. C. Lin, E. Hodapp, H. D. Jampel, J. R. Samples, and S. D. Smith, "Novel glaucoma procedures: a report by the American Academy of Ophthalmology," Ophthalmology **118**(7), 1466–1480 (2011).
56. H. Saheb and I. I. Ahmed, "Micro-invasive glaucoma surgery: current perspectives and future directions," Curr. Opin. Ophthalmol. **23**(2), 96–104 (2012).
57. M. P. Fautsch and D. H. Johnson, "Aqueous humor outflow: what do we know? Where will it lead us?" Invest. Ophthalmol. Vis. Sci. **47**(10), 4181–4187 (2006).
58. R. K. Wang and Z. Ma, "A practical approach to eliminate autocorrelation artefacts for volume-rate spectral domain optical coherence tomography," Phys. Med. Biol. **51**(12), 3231–3239 (2006).
59. American National Standard Institute, Safe use of lasers and safe use of optical fiber communications. New York: ANSI, Z136 committee; 2000:168.
60. S. Makita, Y. Hong, M. Yamanari, T. Yatagai, and Y. Yasuno, "Optical coherence angiography," Opt. Express **14**(17), 7821–7840 (2006).
61. L. An, T. T. Shen, and R. K. Wang, "Using ultrahigh sensitive optical microangiography to achieve comprehensive depth resolved microvasculature mapping for human retina," J. Biomed. Opt. **16**(10), 106013 (2011).
62. S. Asrani, M. Sarunic, C. Santiago, and J. Izatt, "Detailed visualization of the anterior segment using fourier-domain optical coherence tomography," Arch. Ophthalmol. **126**(6), 765–771 (2008).
63. C. G. Caro and D. A. McDONALD, "The relation of pulsatile pressure and flow in the pulmonary vascular bed," J. Physiol. **157**, 426–453 (1961).
64. S. Solomon, S. D. Katz, W. Stevenson-Smith, E. L. Yellin, and T. H. LeJemtel, "Determination of vascular impedance in the peripheral circulation by transcutaneous pulsed Doppler ultrasound," Chest **108**(2), 515–521

(1995).

65. M. F. O'Rourke, "Pressure and flow waves in systemic arteries and the anatomical design of the arterial system," J. Appl. Physiol. **23**(2), 139–149 (1967).
66. D. A. McDonald, "The relation of pulsatile pressure to flow in arteries," J. Physiol. **127**(3), 533–552 (1955).
67. J. R. Womersley, "Method for the calculation of velocity, rate of flow and viscous drag in arteries when the pressure gradient is known," J. Physiol. **127**(3), 553–563 (1955).
68. D. J. Patel, J. C. Greenfield, Jr., W. G. Austen, A. G. Morrow, and D. L. Fry, "Pressure-flow relationships in the ascending aorta and femoral artery of man," J. Appl. Physiol. **20**(3), 459–463 (1965).
69. M. F. O'Rourke and M. G. Taylor, "Vascular Impedance of the Femoral Bed," Circ. Res. **18**(2), 126–139 (1966).
70. M. F. O'Rourke and M. G. Taylor, "Input impedance of the systemic circulation," Circ. Res. **20**(4), 365–380 (1967).
71. R. K. Wang and L. An, "Multifunctional imaging of human retina and choroid with 1050-nm spectral domain optical coherence tomography at 92-kHz line scan rate," J. Biomed. Opt. **16**(5), 050503 (2011).
72. L. An, P. Li, G. Lan, D. Malchow, and R. K. Wang, "High-resolution 1050 nm spectral domain retinal optical coherence tomography at 120 kHz A-scan rate with 6.1 mm imaging depth," Biomed. Opt. Express **4**(2), 245–259 (2013).
73. R. N. Weinreb and P. L. Kaufman, "Glaucoma research community and FDA look to the future, II: NEI/FDA Glaucoma Clinical Trial Design and Endpoints Symposium: measures of structural change and visual function," Invest. Ophthalmol. Vis. Sci. **52**(11), 7842–7851 (2011).

1. Introduction

Tissue deformation is closely correlated with its biomechanical properties [1–3]. Measurement of tissue deformation permits derivation of several important mechanical parameters, such as strain, strain rate and the elastic modulus (ratio of stress over strain). Many diseases alter the mechanical properties of tissue, indicating that the ability to quantitatively measure tissue motion is valuable for the characterization and monitoring of pathologic processes associated with alterations of elasticity and compliance.

In the 1970s, ultrasound elastography was developed to characterize tissue motion based on ultrasonic speckle signals and their corresponding phase information [1,4]. However, due to the limited spatial resolution of ultrasound, the imaging of soft tissue motion has been generally limited to the organ scale. In addition, the contact nature of ultrasound imaging affects measurement accuracy, thereby limiting feasibility in many clinical situations.

Optical coherence tomography (OCT) is capable of cross-sectional imaging of biological tissue in real time with high resolution (<10μm axially) in a noncontact, noninvasive manner [5–7]. In 1998, OCT was first proposed for imaging tissue motion/deformation based on pixelated OCT images, which was generically termed optical coherence elastography (OCE) [8]. Since then, intense efforts have been devoted to exploring OCE's ability to image tissue deformation [9–20]. A variety of methods have been developed in OCE for the purpose of assessing soft tissue motion based on either the speckle tracking [8–10] or the Doppler principle [11–19]. Of special interest, the phase-based Doppler methods permit quantitative assessment of several physical parameters, such as tissue velocity and strain rate (SR) [11–19].

Phase-resolved OCT (PR-OCT) was initially proposed for measuring the velocity of blood flow by evaluating the phase shift between adjacent OCT A-scan signals [21]. This concept was first applied to characterize tissue Doppler resulting from soft tissue motion in 2006 [11]. The measurable range of tissue motion is bounded at the lower limit by the phase noise due to the OCT system itself and to the heterogeneous property of the tissue [22]. When evaluating the phases of OCT signals, the upper limit is bounded by phase-wrapping. The lower limit determines the minimally detectable tissue motion and thus is a critical system parameter when imaging tissue motion at the nanometer scale, the range encountered with TM tissue motion. When the sample experiences slow dynamic motion in the range of 1 Hertz the tissue Doppler approach is not capable of measuring very limited tissue deformation (<1 μm). This imaging difficulty is particularly apparent in an *in vivo* setting where a fast imaging speed has to be employed [23].

In order to address the limitations imposed by phase noise and phase wrapping, another OCT technique termed phase-sensitive OCT (PhS-OCT) was developed that proved capable

of quantification of tissue motion on the nanometer scale [12, 17, 18]. The PhS-OCT technique applies a phase-resolved Doppler algorithm along the slow scanning axis by means of calculating the phase shift between successive B-frames, demonstrating a capability to resolve velocities of tissue motion as slow as 2.6nm/s [12], a speed well suited for imaging pulse-induced TM motion in the 1 Hz range. This PhS-OCT approach permits in vivo characterization of TM tissue movement with a nanometer level of sensitivity not previously attainable by OCT or other means.

The eye is a unique organ that contains some of the most highly vascularized tissues in the body such as the choroid, retina, ciliary body and iris. Pulsatile ocular hemodynamics results from cardiac-induced pulse waves entering the vascular compartments. Pulsatile changes in the vascular compartments of the eye, especially the choroid, result in cardiac pulse dependent cyclic fluctuations of intraocular pressure (IOP) [24]. Pulse-dependent IOP changes in turn cause pulse waves that impinge on the TM.

According to available knowledge, the TM is able to sense and react to its biomechanical environment such as IOP fluctuations and cyclic IOP changes [25]. For example, cyclic changes in IOP alter conventional aqueous outflow in an ex vivo model [26] and alter TM cell contractility in TM cell monolayers [27]. Mechanical stresses also lead to alterations in gene expression [28–32] as well as changes in cytoskeletal networks [28, 33, 34] and modulation of signal transduction [35, 36].

The composition of extracellular matrix in the trabecular beams and juxtacanalicular space is thought to become abnormal in glaucoma [37–40] and is subject to modulation by mechanical stretching [41–43]. Modulation of ECM composition that controls TM elasticity and compliance may be important to normal function [44]. Studies implicate changes in cell [45–48] and ECM stiffness as probable factors in the glaucoma process. Recent elastic modulus determination in normal and glaucoma has indicated a relationship of increased TM tissue stiffness to OAG [49–51], a change also suggested by clinical studies [52–54].

Based on an understanding of the TM as the location of aqueous outflow resistance, interventions have been designed to bypass these abnormal trabecular tissues. Such interventions envision re-establishing normal rates of aqueous flow into Schlemm's canal (SC) or its collector channels. Interventions include removal of portions of the TM, inserting stents or using a SC suture to tighten the TM [55, 56]. Nevertheless, the current understanding of the TM properties responsible for outflow regulation is quite limited, creating an obstacle to informed development of new diagnostic and surgical procedures [57].

The aqueous outflow structures sense and respond to cyclic mechanical stresses and evidence further suggests these tissues undergo stiffening in glaucoma [53, 54]. Our work using PhS-OCT in an ex vivo primate model system [18], demonstrates pulsatile TM motion in response to experimentally controlled IOP transients. Such ex vivo studies have advantages including systematic control of IOP and pulse amplitude. In addition, ex vivo absence of bulk motion greatly simplifies analysis of nm-scale TM motion. However, whether ex vivo results reasonable reflect the presence of TM motion in living subjects can only be answered by in vivo studies.

Studies in living subjects furthermore offer the opportunity to explore the interaction between the TM motion and normal IOP-induced cyclic mechanical stresses. In vivo TM motion characterization provides an opportunity to improve our understanding of how aqueous outflow is regulated and how that regulation becomes abnormal in glaucoma. Motion of the TM as detected by PhS-OCT in vivo is reflective of TM biomechanical properties necessary to control IOP. No techniques are currently available to determine the in vivo TM properties that determine IOP homeostasis. The potential ability to clinically characterize and monitor in vivo TM biomechanical properties may provide improved mechanistic understanding and guidance for diagnosis, prognosis, monitoring and decision making related to medical and surgical interventions in glaucoma.

In this study, pulsatile TM motion was demonstrated in healthy human subjects and characterized with PhS-OCT. Pulsatile TM tissue motion was further related to the cardiac pulse and age through harmonic analysis. Finally, possible clinical applications resulting from the ability to measure pulse-induced TM motion were considered.

2. Material and methods

2.1 Subjects

Table 1. Demographic and statistical data of the cohort

	Mean ± SD	Range
Subjects	10 (20 eyes) *	
Gender (Female/Male)	6/4	
Age (year)	37.7 ± 12.2	25 to 57
Heart rate (beat/min)	70.3 ± 11.7	52.7 to 86.5

* Both right and left eye of 10 healthy subjects. SD, standard deviation.

Ten healthy subjects with no history of ocular disease were recruited. Data concerning demographic characteristics of the subjects is presented in Table 1. PhS-OCT imaging was conducted on both the right and left eye from each subject. Either the temporal or nasal corneo-scleral limbus was selected as the region of interest (ROI) for each eye. None of the subjects were using ocular medications and none had a history of ocular disease, laser procedures or intraocular surgery. Study approval was obtained from the Institutional Review Board at the University of Washington and informed consent was obtained from all subjects before participation.
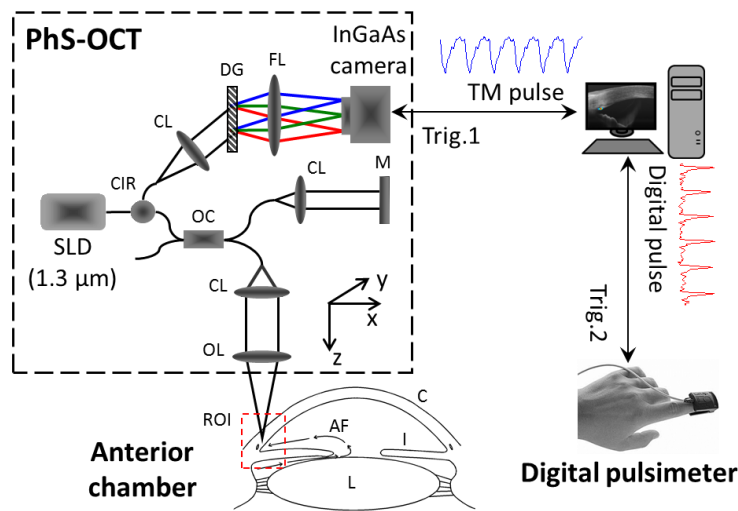

Fig. 1. Schematic diagram of the experimental setup for imaging the anterior segment with PhS-OCT while using a pulsimeter to simultaneously measure the digital pulse signal. Trig.1 triggers PhS-OCT for imaging the TM tissue motion; Trig.2 triggers the digital pulsimeter for recording the digital pulse signal. ROI indicates the OCT imaging area within the corneo-scleral limbus. CIR: circulator; OC: optical coupler; CL: collimating lens; M: mirror; OL: objective lens; DG: diffraction grating; FL: focusing lens; C: Cornea; I: iris; L: lens; AF: aqueous flow.

2.2 System setup

The schematic of the experimental setup used for *in vivo* quantification of ocular tissue motion is shown in Fig. 1. The setup was composed of two primary parts: PhS-OCT for measuring TM tissue motion and a digital pulsimeter (PowerLab, ML866) for recording the

digital pulse signal. An external controlling unit with two triggers was used to synchronize the PhS-OCT images (Trig.1) and the digital/cardiac pulse signals (Trig.2).

The PhS-OCT system is based on a spectral domain OCT (SD-OCT) configuration [18, 58]. A broadband superluminescent light source with a central wavelength of 1340nm and an effective spectral full-width at half-maximum (FWHM) of 110nm was used to achieve an axial resolution (of theoretically ~7.2 μm in air). In the sample arm, an objective lens (focal length of 50mm) was used to focus the probing light beam on the region of interest (ROI), i.e. the corneo-scleral limbus, yielding a measured lateral resolution of ~16μm. The OCT detection unit was a high-speed spectrometer, equipped with an InGaAs line scan camera capable of ~92 kHz A-line scan rate. The spectrometer had a spectral resolution of 0.14 nm providing a measured imaging depth of ~3.0 mm in air. The system dynamic range was measured at ~105 dB at the depth-position of 0.5 mm with an incident optical power of 2.5 mW at the sample. This incident light power is within the safe ocular exposure limits recommended by the American National Standards Institute (ANSI) [59].

In addition, the digital pulsimeter was equipped with a piezo-electric transducer to convert the finger blood pressure pulse into an electrical analog signal.

2.3 Data acquisition and processing

For each eye, 1000 repeated OCT B-frames (MB-mode scan protocol, 360 A-lines per B-frame, ~200 frames per second, ~5 seconds per data set) were captured at one spatial location at the corneo-scleral limbus (as indicated by the ROI in Fig. 1); by means of a trigger, the digital pulse-wave signal $P_d(t)$ was recorded concurrently. From the PhS-OCT data set, a time sequence of structural cross-sections based on the OCT amplitude signal was generated [refer to Fig. 2(A)].

From the sequence of OCT B-frame images, the phase-shift between adjacent B-frame was evaluated by the use of a PhS-OCT algorithm to represent the instantaneous velocity of tissue movement $V_t(x,z,t)$ [12, 18]. Due to involuntary movement of the human eye and head [60, 61], a phase compensation procedure was implemented to remove the bulk tissue motion between B-frames. Assuming that the bulk motion induces a phase change of $\Delta\varphi_{bulk}(x,z,t)$, the phase-shift due to the localized motion can be obtained by compensating $\Delta\varphi_{bulk}(x,z,t)$:

$$\varphi(x,z,t) = \arg\left(r(x,z,t-\tau)r^*(x,z,t)\exp[-\Delta\varphi_{bulk}(x,z,t)]\right) \tag{1}$$

where $r(x,z,t)$ is the complex OCT signal at time t, τ is the time interval between the adjacent B-frames, and * is used to denote complex conjugation for complex signal. In the results reported below, we determined $\Delta\varphi_{bulk}(x,z,t)$ by a histogram-based approach [60, 61]. Accordingly, a time sequence of corrected TM velocity cross-sections was readily generated [refer to Fig. 2(B)]:

$$V_t(x,z,t) = \frac{\lambda_0}{4\pi n\tau}\varphi(x,z,t) \tag{2}$$

where λ_0 is the central wavelength of the light source, and n is the refractive index of the sample that is typically 1.38 for most soft tissues.

As a result of the eye motion, a lateral and axial displacement between the MB-mode B-frames was present. To facilitate extraction of the instantaneous TM velocity $V_t(x_0,z_0,t)$ for a specific spatial position (x_0,z_0), an algorithm based on 2D cross-correlation was developed that permitted spatial alignment of all the B-frames of each data set. The first B-frame at time t_0 was used as the reference frame. The lateral and axial shift (Δx and Δz) of the B-frame at time t was determined by maximizing the 2D cross-correlation $\gamma(\Delta x, \Delta z, t)$:

$$\gamma(\Delta x, \Delta z, t) = \frac{\left| \sum_{x,z} \left[r^*(x, z, t_0) r(x + \Delta x, z + \Delta z, t) \right] \right|}{\sqrt{\sum_{x,z} |r(x, z, t_0)|^2} \sqrt{\sum_{x,z} |r(x + \Delta x, z + \Delta z, t)|^2}} \tag{3}$$

Based on the calculated Δx and Δz at time t, all the B-frames are then aligned for further processing.
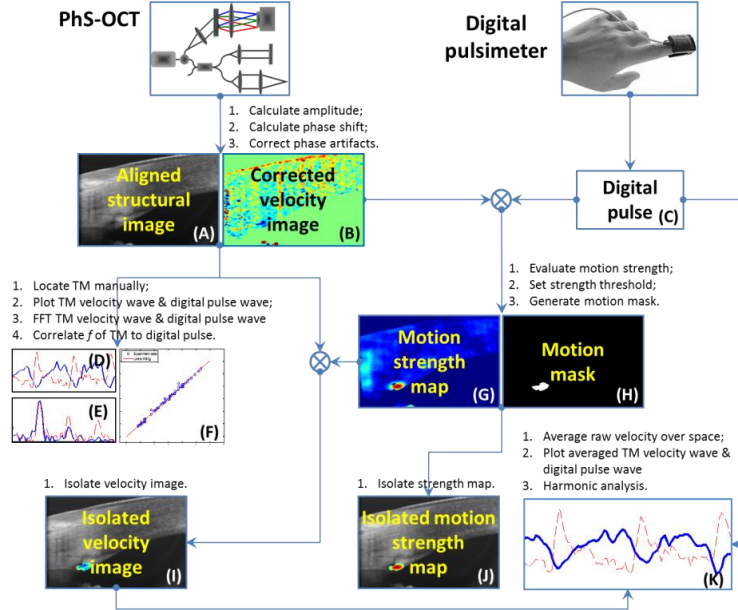
Fig. 2. Flow chart of PhS-OCT signal processing. In (D), (E) and (K), solid blue curve represents TM velocity wave $V_t(t)$ and dashed red curve represents digital pulse wave $P_d(t)$.

In the OCT structural imaging, the TM appears typically as a "triangular" structure with the base attached at the scleral spur [62]. Based on this morphological feature, the TM region can be identified in each of the structural and velocity cross-sections. A 3x3 pixel square centered at position (x_0, z_0) is then placed on the TM. Using the above experimental setup, the instantaneous TM velocity wave $V_t(t)$ was defined as:

$$V_t(t) = \frac{\sum_{l=-1}^{1} \sum_{m=-1}^{1} V_t(x_0 + l, z_0 + m, t)}{9} \tag{4}$$

where l and m are integers. Consequently, a pair consisting of the TM velocity wave $V_t(t)$ and the simultaneous digital pulse wave $P_d(t)$ was available for each data set [refer to Fig. 2(D)]. Taking the Fourier transform of each of the wave forms permits identification of the frequency components in their respective power spectra [refer to Fig. 2(E)].

Based on Fourier analysis of real functions, the instantaneous digital/cardiac pulse wave $P_d(t)$ can be resolved into a series of harmonic terms $P_{di}(t)$ in the frequency domain [63–65] [refer to Fig. 2(D) and 2(E)]:

$$P_d(t) = P_{d0} + \sum_{i=1}^{n} P_{di}(t)$$
$$P_{di}(t) = a_{di} \cos(2i\pi f t) + b_{di} \sin(2i\pi f t) \tag{5}$$

where the coefficients a_{di} and b_{di} are the amplitude of the cosine and sine wave components at a given harmonic frequency $i*f$; where $i = 1, 2, ..., n$ is a positive integer (the harmonic number) and f is the fundamental frequency equivalent to the heart rate. P_{d0} is the temporal

mean value of the function. It is documented that most energy in an arterial pulse wave is contained within the first five harmonic components [65]. To be conservative, we elected to use about twice the number of harmonic terms for the following analysis, i.e. $n = 9$.

From the power spectrum, the frequency contents of the TM velocity wave and the digital/cardiac pulse wave were correlated based on Pearson's linear correlation approach. Due to the significant correlation between the frequency components of the TM velocity wave and the digital/cardiac pulse wave [refer to Fig. 2(F)], the instantaneous TM velocity wave $V_t(t)$ can also be decomposed into a series of harmonic terms $V_{ti}(t)$ in a manner similar to that used to resolve the digital/cardiac pulse:

$$V_t(t) = V_{t0} + \sum_{i=1}^{n} V_{ti}$$
$$V_{ti}(t) = a_{ti} \cos(i\,2\pi ft) + b_{ti} \sin(i\,2\pi ft)$$

(6)

Where, the coefficients a_{ti} and b_{ti} are the amplitude of the cosine and sine wave components at a given harmonic frequency $i*f$. V_{t0} is the temporal mean value of the function; also $n = 9$. Finally, to facilitate further characterization of TM motion, a procedure was developed to semi-automatically isolate the TM pulsatile motion from the corrected TM velocity images by the following means: [refer to Figs. 2(B), 2(C), 2(G)-2(K)]

1) **Evaluate motion strength**: Because the measurements were dominated by the first 3 harmonics in all the cases we studied, we elected to use these harmonics to determine the TM motion strength. Thus, the coefficients a_{ti}, b_{ti} and the magnitude M_{ti} were calculated at the frequencies $1f$, $2f$, and $3f$ for each data set where f was the heart rate determined from the corresponding digital/cardiac pulse wave $P_d(t)$:

$$a_{ti} = \tfrac{\tau}{2} \int_{-T/2}^{T/2} V_t(t) \cos(2\pi ift)dt$$
$$b_{ti} = \tfrac{\tau}{2} \int_{-T/2}^{T/2} V_t(t) \sin(2\pi ift)dt$$

(7)

The magnitude M_{ti} of the TM velocity wave for each harmonic frequency can be expressed as:

$$M_{ti} = \sqrt{a_{ti}^2 + b_{ti}^2}$$

(8)

The TM motion strength S_t was defined as the summation of the magnitude of the first three harmonics [refer to Fig. 2(G)]:

$$S_t = \left(M_{t1} + M_{t2} + M_{t3} \right)$$

(9)

2) **Set motion strength threshold and generate a motion mask** by binarizing the motion strength map: setting $1/e$-maximum as the threshold, where $e = 2.71828$ is the natural constant [refer to Fig. 2(H)].

3) **Isolate TM motion strength** [refer to Fig. 2(J)] from the motion strength map (Fig. 2(G)) using the motion mask (Fig. 2(H)).

4) **Isolate TM velocity** [refer to Fig. 2(I)] from the corrected velocity image (Fig. 2(B)) using the motion mask (Fig. 2(H)).

2.4 Harmonic analysis

Harmonic analysis has been widely used for quantification of the dynamic pressure-flow relationship in the arterial system; the resulting data is commonly termed input impedance [66–70]. In this study, instantaneous pressure and TM motion were simultaneously recorded and digitized for spectral or Fourier analysis. The sinusoidal pressure harmonic was then

related to its corresponding TM harmonic and quantified by two parameters: a modulus of maximal wave magnitude and a phase. The modulus is the ratio of the greatest magnitude of the sinusoidal pressure wave to the corresponding sinusoidal TM motion wave. The phase is the phase angle of pressure less that of TM motion.

Because TM tissue motion results from pulse-induced ocular hemodynamics, the correlation between the cardiac pulse and TM tissue motion may provide important insights into aqueous outflow system physiology. By an analogy similar to that used in the quantification of pressure-flow relationship in the arterial system [66–70], the cardiac pulse and tissue motion relationship was quantified in this study. Due to its reasonable cost, availability and widespread clinical use, a digital pulsimeter was chosen for the measurement of the timing of the cardiac pulse waves. Calculations were made of the phase lag $\Delta\theta_i$ between the digital pulse harmonics and the corresponding TM tissue motion harmonics for each pair of data sets:

$$\Delta\theta_i = \theta_{di} - \theta_{ti} \tag{10}$$

The phase of the digital pulse wave θ_{di} and the phase of TM motion θ_{ti} for each harmonic frequency can be respectively calculated as:

$$\theta_{di} = \tan^{-1}\left(\frac{b_{di}}{a_{di}} \right)$$
$$\theta_{ti} = \tan^{-1}\left(\frac{b_{ti}}{a_{ti}} \right) \tag{11}$$

Accordingly, the time delay Δt_i between the digital pulse harmonic and the simultaneous tissue motion harmonic can be written as:

$$\Delta t_i = \frac{\Delta\theta_i}{2\pi i f} \tag{12}$$

2.5 Statistical analysis

All data were analyzed with statistical analysis software (SPSS, version 18; SPSS Inc., Chicago, IL). Correlation analysis was performed to assess the relationship of phase lag $\Delta\theta_i$ with that of the heart rate and age. The results of correlation are expressed as a *P* value for the null hypothesis tests and a R^2 value for the Pearson's linear correlation coefficient. For all analysis, a *P* value < 0.05 was considered to be statistically significant.

2.6 Pulsatile blood flow in the central retinal artery

In the current study, the digital pulse wave was recorded by measuring the blood pressure pulse in the finger with a pulsimeter. The measured digital pulse wave was used to indicate the timing of cardiac pulse and to provide a reference for characterizing pulsatile TM motion. To assess whether the digital pulse provides an appropriate timing reference, we performed a separate experiment, correlating the digital pulse wave with the cardiac pulse wave recorded from the central retinal artery (CRA). In doing so, we used a 1050nm SDOCT system designed for posterior segment imaging [71, 72] to image the central retinal artery located at the optic nerve head.

During imaging, the system operated in the M-mode with a scan speed set at 200 frames per second. We captured a series of M-mode OCT cross-sectional images over a 5 sec duration to cover approximately 5 cycles of the cardiac pulse, while we simultaneously recorded the digital pulse wave from the pulsimeter. From the M-mode scan images, a PR-OCT algorithm was applied to obtain the corresponding blood flow image, from which images the axial velocity of blood flow in the CRA was evaluated over the 5 sec duration.

3. Results

3.1 Temporal and frequency relationships between cardiac pulse and TM motion

Figure 3(A) is a representative structural cross-section of the corneo-scleral limbus, in which important morphological features of the aqueous outflow system can be appreciated, such as the TM, SC, collector channel (CC) etc. Referring to the structural cross-section, the TM region is readily located in the corresponding velocity cross-section (Fig. 3(B)). The instantaneous velocity of the non-TM tissue selected from the corneal regions [marked by the black thin arrows in Figs. 3(A) and 3(B)] is plotted over time in Fig. 3(C). Similar results (data not shown) were obtained from other non-TM tissues, for example the scleral and conjunctival regions. The instantaneous velocity wave of the TM tissue [marked by the red bold arrows in Figs. 3(A) and 3(B)] is plotted in Fig. 3(D). In Figs. 3(C) and 3(D), the concurrently recorded digital pulse wave is also displayed for comparison.

Figure 3 makes it clear that the instantaneous velocity at the non-TM tissue regions has random appearance. Spectral and Fourier analysis did not show any sign of periodicity. In contrast to the non-TM velocity, the TM velocity wave qualitatively exhibits an apparent periodicity with the same oscillatory rhythm as the digital pulse wave, i.e. the heart rate. Furthermore, the analysis of their power spectra (Fig. 3(E)) indicates that the energy of both the pulsatile waves is mainly concentrated in the same frequency components, i.e. several similarly distributed harmonic frequency patterns. Both of the above-mentioned temporal and frequency characterizations were further confirmed in the quantitative statistical analysis (total of 20 eyes).
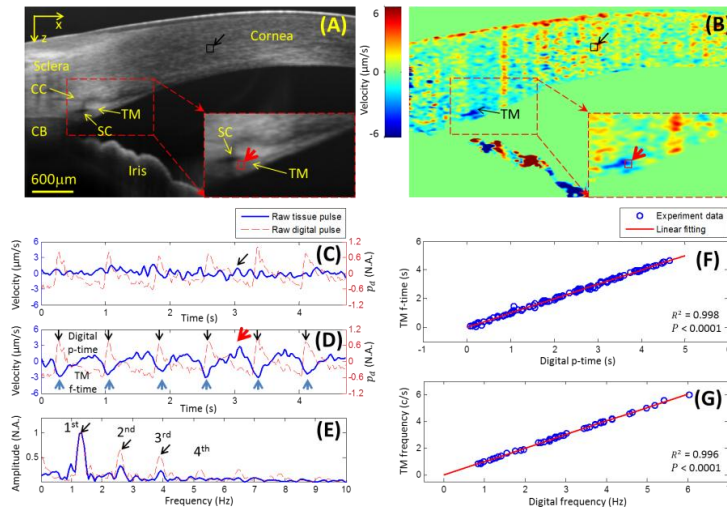

Fig. 3. Temporal and frequency characterization of TM motion. (A) Representative OCT microstructural cross-section of the corneo-scleral limbus, insert is an enlarged view of TM and SC region as marked by the dashed red square in (A); (B) Corresponding representative velocity image with bulk motion corrected; insert is an enlarged view of TM and SC region as marked by the dashed red square in (B); (C) Instantaneous tissue velocity wave captured from a 3x3 pixel square on the cornea as marked by the black thin arrow in (A) and (B) together with the simultaneous digital pulse wave $P_d(t)$; (D) Instantaneous tissue velocity wave $V_t(t)$ captured from a 3x pixel square over the TM as marked by the red bold arrow in (A) and (B) together with the simultaneous digital pulse wave $P_d(t)$ (E) Power spectrum of the TM velocity wave $V_t(t)$ and the simultaneous digital pulse wave $P_d(t)$ reported in (D); (F) Linear correlation between the TM f-time and the digital p-time; (G) Linear correlation of the frequency components of the TM velocity wave and the digital pulse wave. CC: collector channel, SC: Schlemm's canal, TM: trabecular meshwork, CB: ciliary body, Digital p-time: instantaneous time of digital pulse peak, TM f-time: instantaneous time of the TM velocity pulse minimum.

Figure 3(F) demonstrates the significant correlation ($R^2 = 0.998$, $P<0.0001$) of the instantaneous time between the digital pulse peaks [digital p-time, marked by black thin arrows in Fig. 3(D)] and the TM pulse minima [TM f-time, marked by blue bold arrows in Fig. 3(D)]. The results demonstrate the temporal synchronization between the cardiac pulse and the TM motion with an evident phase lag. The chart in Fig. 3(G) illustrates the significant correlation ($R^2 = 0.996$, $P<0.0001$) of the frequency components.

3.2 Spatial characterization of TM motion

Figure 4(A) is the normalized motion strength map of the ocular tissue motion at the corneo-scleral limbus generated according to Eqs. (7)-(9), demonstrating that the TM region exhibits a strong pulsatile motion containing the same frequency components as the digital/cardiac pulse. By setting a *1/e*-maximum (~0.37 for normalized strength mapping) as the strength threshold and generating a motion mask [as shown in Fig. 2(H)], the TM pulsatile motion can be isolated. Figure 4(B) shows the isolated TM strength map superimposed onto the corresponding structural cross-section. The insert suggests that the strongest motion center is located in the area of the trabecular wall of SC, gradually dampening from the center out to the periphery. Figures 4(C) and 4(D) show the isolated TM velocity cross-sections superimposed on the structural cross-section, which respectively correspond to the downward velocity toward the anterior chamber during the decrease of the IOP and the upward velocity toward SC external wall during the increase of the IOP.
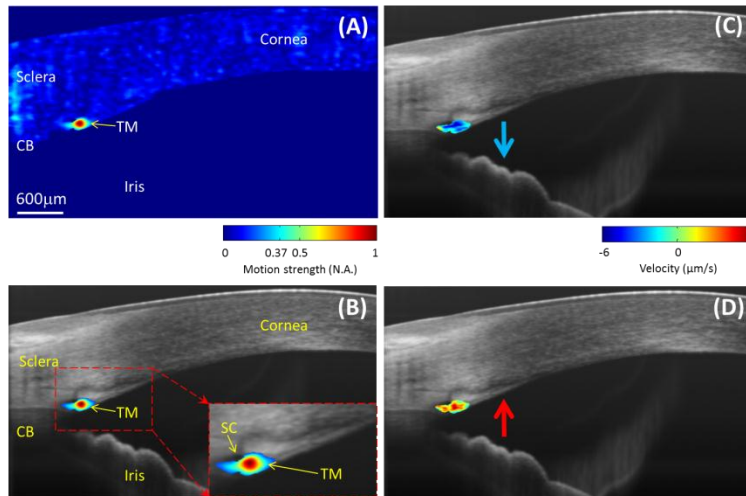

Fig. 4. Spatial characterization of TM motion. (A) Normalized strength mapping of the ocular tissue motion around the corneo-scleral limbus; (B) isolated TM strength mapping superimposed on the corresponding structural cross-section, enlarged view of the area marked by the dashed red square in (B); (C) and (D) isolated TM velocity cross-sections superimposed on the structural cross-section, respectively corresponding to the downward velocity toward the AC and the upward velocity toward SC external wall.

3.3 Decomposition of TM motion

Figure 5(A) plots the averaged magnitude M_{ti} (20 human eyes) of the TM velocity wave versus the harmonic frequencies (cycles per second), revealing that the energy of the TM motion is mainly contained in the first 3 harmonic frequencies. Figures 5(B)-5(E) depict the harmonic decomposition of a representative TM velocity wave and its corresponding digital/cardiac pulse wave into the first 4 harmonic waves. For each harmonic component, an obvious phase lag $\Delta\theta_i$ is present.

The relationships between phase lag $\Delta\theta_i$, heart rate and age were assessed and are presented in Fig. 6. Generally, the phase lag $\Delta\theta_i$ decreases with the increase of the heart rate and the age. A significant linear relationship ($P<0.05$) can be found in $\Delta\theta_1$ and $\Delta\theta_3$ versus the heart rate. The phase lag $\Delta\theta_i$ is primarily distributed around 2-4 rad for all the first 4 harmonic components. The specific mean values of $\Delta\theta_i$ are listed in Table 2. From this result, the time delay Δt_i can be readily obtained by using Eq. (12). The mean values of Δt_i are listed in Table 3. The time delay Δt_1 ranges from ~0.3-0.7s with a mean value of ~0.5s.
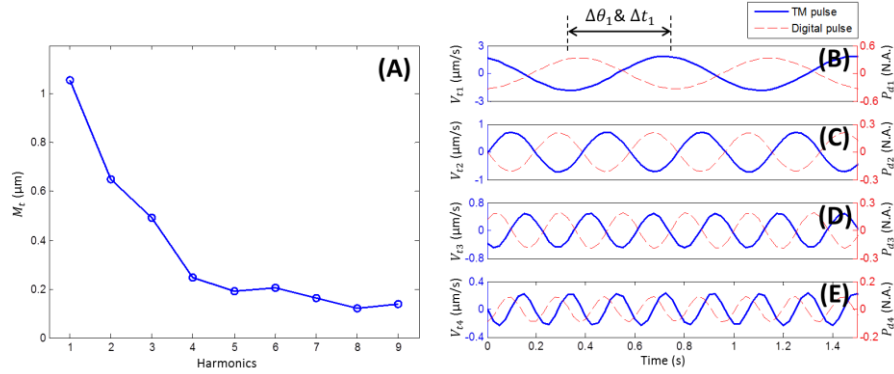

Fig. 5. Decomposition of TM motion. (A) Magnitude M_{ti} of the TM velocity wave versus the first 9 harmonic frequencies; (B-E) first 4 harmonic components of the TM velocity wave (blue curve) and the digital pulse wave (red curve).
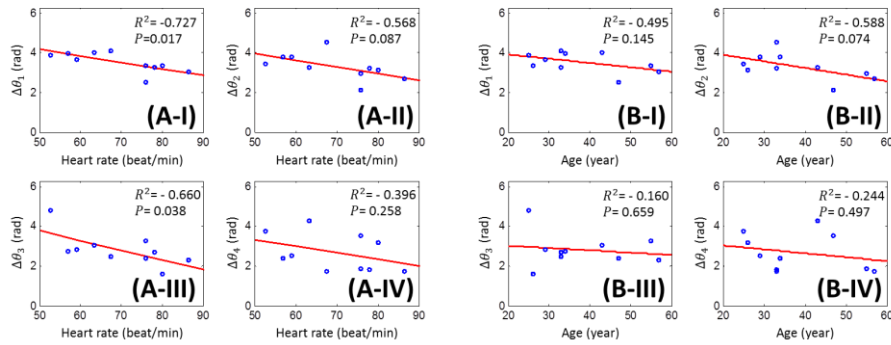

Fig. 6. Scatter plot of phase lag $\Delta\theta_i$ (i = 1,2,3,4) versus heart rate (A) and age (B). Red trend lines describe the generally negative statistical relationships.

Table 2. Mean phase lag $\Delta\theta_i$ (i = 1,2,3,4).

	$\Delta\theta_1$ (rad)	$\Delta\theta_2$ (rad)	$\Delta\theta_3$ (rad)	$\Delta\theta_4$ (rad)
Mean ± SD	3.53 ± 0.48	3.31 ± 0.63	2.82 ± 0.80	2.69 ± 0.89

Table 3. Mean time delay Δt_i (i = 1,2,3,4).

	Δt_1 (s)	Δt_2 (s)	Δt_3 (s)	Δt_4 (s)
Mean ± SD	0.50 ± 0.14	0.24 ± 0.07	0.14 ± 0.06	0.10 ± 0.04

3.4 Pulsatile blood flow in central retinal artery

Figure 7 shows the velocity pulse wave of CRA measured by the 1050nm SDOCT system. Figure 7(A) is a representative structural cross-section of the optic nerve heard, in which an artery and a vein can be readily identified. Figure 7(B) and 7(C) are the enlarged view of the structural and corresponding velocity images, respectively. As shown in Fig. 7(D), the axial

velocity pulse wave of blood flow in CRA and the digital pulse wave are synchronized. Figure 7(C) reports the 1st harmonic waves of both the CRA pulse and the digital pulse using the harmonic analysis method. It can be seen that the 1st harmonic waves of both the CRA pulse and the digital pulse are almost in phase (with a ~0.54 rad phase lag and ~0.08 s time delay).

4. Discussion

Pulse- induced TM motion can be quantitatively assessed using the currently described PhS-OCT system that is synchronized with a digital pulsimeter and uses a phase compensation algorithm to remove bulk tissue bulk motion. By comparison with reference locations inthe corneal, conjunctival and scleral tissues, it is apparent that the TM exhibits pulsatile motion along the direction of the Doppler probe beam [refer to Fig. 4(A)]. Furthermore, such pulsatile TM motion is significantly correlated with the digital/cardiac pulse; in fact, the motion is precisely synchronized except for the presence of a phase lag [refer to Figs. 3(D) and 3(F)]. Energy of both the cardiac pulse and TM motion is concentrated primarily in the same frequency components [refer to Figs. 3(E) and 3(G)]. Thus, pulsatile TM motion is most likely due to ocular hemodynamics, particularly cardiac-induced oscillations of the IOP [18, 44, 52, 53].
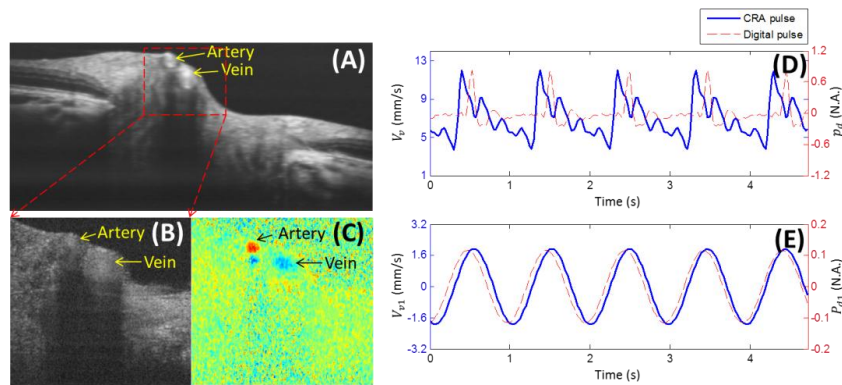

Fig. 7. Velocity pulse wave of CRA measured by the 1050nm SDOCT system. (A) a typical OCT image crossing the optic nerve head; (B) enlarged field-of-view of the area marked by the red square in (A) and (C) the corresponding Doppler velocity color map, from which the Doppler velocity of the CRA is calculated in the M-B scans. (D) Instantaneous Doppler velocity of the pulsatile blood flow in the CRA over ~5sec duration and the corresponding digital pulse wave concurrently recorded; (E) the 1st harmonic wave of the CRA pulse and the simultaneous digital pulse evaluated from the signals in (D).

The phase lag $\Delta\theta_i$ between the pulsatile TM motion and the digital pulse was negatively correlated with heart rate and age respectively. A linear relation reached significance for heart rate but not for age. A larger data set including a broader age range may provide a clearer picture of the significance of age. In addition, other ocular parameters such as differing IOPs, axial length of the globe and scleral rigidity were not addressed and are factors which may also play an important role.

In this study, we used the digital pulse wave as the reference to characterize the measured pulsatile TM motion. However, it seems obvious that such an analysis should be based on the IOP, rather than the digital pulse wave as the reference [18, 44, 52, 53]. The invasive procedure required to provide continuous measurement of pulse-dependent IOP prevented us from using this latter approach in the current in vivo human study. Because the IOP pulse is directly correlated with ocular hemodynamics [24], we elected to measure the pulse wave in the central retinal artery, a vessel easily accessible for OCT imaging. Simultaneous measurements of CRA and digital pulse waves permitted direct correlation between the ocular

and digital pulse temporal relationships. We reasoned that a strong temporal correlation would make our decision to use the digital pulse as the reference for pulse-induced TM movement acceptable. Our measurement results (Fig. 7) show that this correlation is indeed high with a negligible phase lag. We also observed that the phase lag $\Delta\theta_i$ and time delay Δt_i between the pulsatile TM motion and the digital pulse is roughly equivalent to the corresponding phase lag and time delay between TM motion and the CRA pulse. Accordingly, digital pulse wave timing appears to be a reasonable surrogate for ocular pulse wave timing.

In this pilot study the absolute and directional TM motion is difficult to assess precisely. This difficulty is in part due to our limited understanding of how pulse-induced vector forces affect this tissue with its highly complex organization, and in part due to the employed PhS-OCT system that is only sensitive to the tissue motion along the probe beam direction. Accordingly, the Doppler angle correction was neglected in calculating the TM motion velocity. Because of the unknown influence of the Doppler angle, the velocity amplitude of the TM motion was not included in the statistical analysis.

In future efforts, we intend to expand our previous studies of pulse-induced TM motion in enucleated monkey eyes to include enucleated human eyes where motion artifact is absent, thus improving actual system sensitivity to TM motion. In enucleated eyes we will experimentally control pulse frequencies, amplitudes and IOPs to characterize their effect on TM motion. The controlled parameters with improved measurement sensitivity in *ex vivo* preparations should permit better characterization of vector forces associated with pulse-induced TM motion. Implementation of technical improvements along with *ex vivo* studies can further define TM biomechanics and provide better tools for future *in vivo* assessment of TM motion parameters.

Such an optimized system should be capable of deriving absolute and directional TM motion. Quantitation of TM motion permits characterization of the underlying biomechanics that determine the outflow system's ability to maintain IOP homeostasis. Characterization of these biomechanical properties may provide structural and functional endpoint parameters [73] useful in the management of IOP, the most critical risk factor in glaucoma.

5. Conclusion

This study provides evidence of trabecular meshwork motion induced in vivo by the cardiac pulse, a tissue behavior not previously recognized. In this study we have used phase sensitive optical coherence tomography (PhS-OCT) to detect and quantify pulse-induced TM motion in humans. From the experimental results, we observed that in vivo pulsatile TM motion is correlated with the cardiac pulse, which is responsible for pulsatile intraocular pressure (IOP) oscillations.

Motion of the TM is affected by parameters such as heart rate and age. However, it should be noted that our conclusions are based upon a limited number of observations (10 subjects, 20 eyes) enrolled in this study. Future studies will increase the number of subjects providing us with increased data and statistical power from which to draw conclusions. We have also shown that the PhS-OCT system provides a new technology for in vivo characterization of the biomechanical properties of the TM, properties that become abnormal in glaucoma. The noninvasive, noncontact system described in this report thus may hold promise as a clinical tool in the management of glaucoma.

Acknowledgement